

On the second law of thermodynamics: Spontaneous cold-to-hot heat transfer in a nonchaotic medium

Yu Qiao^{1,2,*}, Zhaoru Shang¹

¹ Program of Materials Science and Engineering, University of California – San Diego, La Jolla, CA 92093, U.S.A.

² Department of Structural Engineering, University of California – San Diego, La Jolla, CA 92093-0085, U.S.A.

* Corresponding author (email: yqiao@ucsd.edu)

Abstract: It has long been known that, fundamentally different from a large body of rarefied gas, when a Knudsen gas is immersed in a thermal bath, it may never reach thermal equilibrium. The root cause is nonchaoticity: as the particle-particle collisions are sparse, the particle trajectories tend to be independent of each other. Usually, this counterintuitive phenomenon is studied through kinetic theory and is not considered a thermodynamic problem. In current research, we show that if incorporated in a compound setup, such an intrinsically nonequilibrium behavior has nontrivial consequences and cannot circumvent thermodynamics: cold-to-hot heat transfer may happen spontaneously, either continuously (with an energy barrier) or cyclically (with time-dependent entropy barriers). It allows for production of useful work by absorbing heat from a single thermal reservoir without any other effect. As the system obeys the first law of thermodynamics, the refrigeration statement and the heat-engine statement of the second law of thermodynamics cannot be applied. The basic principle of maximum entropy is adhered to.

Keywords: Nonchaoticity; nonequilibrium; heat transfer; the second law of thermodynamics; Knudsen gas

1. Introduction

An ideal gas (e.g., a classical rarefied gas) is referred to as a Knudsen gas when the mean free path of the gas particles (λ_F) is larger than the characteristic size of the gas container (D) [1], as depicted in Figure 1(a-c). Because $D < \lambda_F$, compared to the particle-wall collisions, the particle-

particle collisions are sparse, so that their effect is secondary. In the interior of the container, the particle trajectories tend to be nonchaotic [2]. As a result, the conventional thermodynamic analysis methods, such as the Bhatnagar-Gross-Krook (BGK) model for the Boltzmann equation [3], may not be applicable. Usually, a Knudsen gas is studied through kinetic theory, not through statistical mechanics. It could have unique fluid dynamic properties (e.g., the Knudsen paradox [4]) and unusual thermal properties (e.g., the Knudsen effect [5]). In mesoscopic physics, somewhat similar nonequilibrium phenomena are also observed, e.g., the ballistic transport of charge carriers [6].

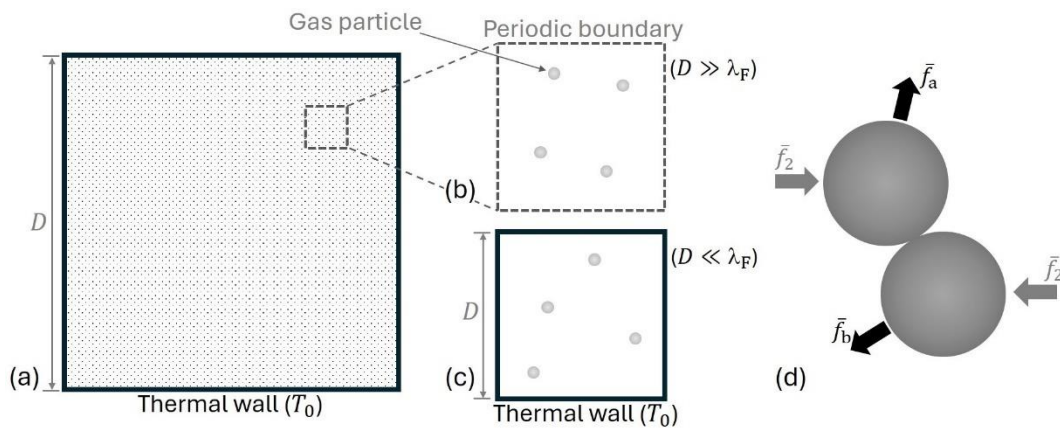


Figure 1. (a) A chaotic ideal gas (e.g., a large body of rarefied gas) immersed in a thermal bath. The container size (D) is much larger than the mean free path of the gas particles (λ_F). The container boundaries are made of thermal walls. (b) A small volume of the ideal gas in panel (a) may be modeled by using periodic boundary condition. (c) A Knudsen gas immersed in a thermal bath. The container boundaries are made of thermal walls, fundamentally different from panel (b). When $D \ll \lambda_F$, in the interior of the container, the particle trajectories tend to be nonchaotic. Compared to the particle-wall collisions, the particle-particle collisions are sparse, and their effect is secondary. Consequently, the steady-state gas-phase kinetic temperature (T) is lower than the thermal-wall temperature (T_0), i.e., the system cannot relax to thermal equilibrium. (d) Boltzmann's H-theorem is the foundation of the second law of thermodynamics. It is based on the assumption of molecular chaos, which requires extensive particle-particle collisions throughout the system. Before two particles randomly collide, their state is governed by the two-body probability density (\bar{f}_2); after the collision, \bar{f}_2 is replaced by $\bar{f}_a \cdot \bar{f}_b$, where \bar{f}_a and \bar{f}_b are the one-body probability densities of the two particles, respectively. The information loss breaks time symmetry of the evolution of the probability of system state. Thus, although all the governing equations are time-reversible, entropy increase is irreversible. In the Knudsen-gas models in current research, however, particle-particle collisions are sparse, so that the H-theorem is inapplicable.

People are well aware that when a Knudsen gas is immersed in a thermal bath, it may never reach thermodynamic equilibrium [7,8]. Specifically, at the steady state, the effective gas-phase kinetic temperature ($T \propto \bar{K}/k_B$) can be significantly lower than the container-wall temperature (T_0) [9-11], where \bar{K} is the average particle kinetic energy, and k_B is the Boltzmann constant. This

is because, without extensive particle-particle collisions, the fast gas particles tend to rapidly move across the container, while the slow gas particles tend to stay long in the interior. At any moment, compared to thermal equilibrium, it is more likely to find slow particles in the Knudsen gas, and less likely to find fast particles. One perspective to understand this counterintuitive phenomenon is to examine the extreme case wherein the container contains only one gas particle. Because it is impossible for the particle to encounter another particle, the effective mean free path of particle-particle collision $\lambda_F \rightarrow \infty$. The mean free path of particle-wall collisions may be assessed as $\lambda_w = \pi D/4$ [12]. Since $\lambda_w \ll \lambda_F$, the system behavior is dominated by the particle-wall collisions. As the container walls are in contact with the thermal bath, the probability density (ρ_L) of finding the particle at speed v is proportional to $p_w(v)/v$, where p_w is the Maxwell-Boltzmann distribution of particle speed (v) at T_0 . In the ideal-case scenario, with the non-Boltzmann $\rho_L \propto p_w/v$, $T = T_0/2$ for a two-dimensional Knudsen gas and $T = 2T_0/3$ for a three-dimensional Knudsen gas (See Section A1 in the Appendix for the detailed discussion). It is worth noting that Knudsen gas is fundamentally different from many-body localization (MBL) [13]. MBL studies a subregion with a given initial condition and nontrivial particle interactions; if the subregion is exposed to a thermal reservoir, through unbiased sampling of the initial state, the ensemble average of an observable would be equal to the equilibrium value predicted by quantum statistical mechanics.

In the past, Knudsen gases were studied in simple setups, without external force fields (energy barriers) or time-dependent hurdles of particle-particle collision (entropy barriers). Under this condition, the intrinsically nonequilibrium steady state ($T < T_0$) was viewed as “trivial”, partly because T can be theoretically calculated but cannot be directly measured. If a temperature sensor is used, the measurement result at the sensor-gas interface would be the container-wall temperature (T_0), compatible with the zeroth law of thermodynamics.

However, recent research on spontaneously nonequilibrium dimension (SND) [14-16] raises a critical question: what if a Knudsen gas is combined with an energy barrier or a time-dependent entropy barrier? Such a concern is reinforced by the fact that Boltzmann’s H-theorem [3] is inapplicable to a Knudsen gas, since the assumption of molecular chaos is irrelevant (see Figure 1d). In the nonchaotic setup in Figure 1(c), there is no kinetic mechanism for entropy to increase to the equilibrium maximum (S_{eq}). The theoretical analyses in [14,15] demonstrated that, with locally nonchaotic energy barriers, there are macroscopic non-thermodynamic systems having nontrivial energy properties. They can produce useful work in a cycle by absorbing heat

from a single thermal reservoir without any other effect. The numerical and experimental study in [16] drew a similar conclusion for locally nonchaotic time-dependent entropy barriers, as entropy spontaneously decreased without an energetic penalty.

In Sections 2 and 3 below, case studies are performed on heat transfer in two Knudsen-gas-enabled models. In Section 2, a Knudsen gas is placed in a gravitational field, similar to the low-height energy barriers in [14,15]. In Section 3, by using switchable inner walls as time-dependent entropy barriers, a Knudsen-gas cell cluster is cyclically converted to a chaotic ideal gas. The results are discussed in Sections 4-6.

Hereafter, the term “nonequilibrium” (or “intrinsically nonequilibrium”) refers to a steady state that is spontaneously different from thermodynamic equilibrium, without an external driving force. The system is closed and, unless otherwise specified (e.g., Section 2.2), isothermal (i.e., immersed in a thermal bath). The study is in the framework of classical mechanics and mainly numerical. The computer programs are available at [17].

2. The first model: a Knudsen gas in gravity

Previously, people extensively studied heat transfer either in a nonchaotic medium without gravity [18-21] or in gravity for a chaotic medium [22-24]. For instance, when the system height (D) is much larger than the particle mean free path (λ_F), the planar Fourier flow associated with the chaotic particle movements fits well with the BGK model, and the average gas-phase temperature equals to the average temperature of the environment. In this section, we investigate a model wherein not only the medium is nonchaotic ($D \ll \lambda_F$) but also the gravity effect is nontrivial, critically distinct from the conventional cases.

2.1 Thermally nonequilibrium steady state in a thermal bath

Figure 2(a) shows a Monte Carlo (MC) simulation of a two-dimensional (2D) gas, wherein a number of billiard-like particles randomly move in a uniform gravitational field (g) in a vertical plane. The 2D gas particles are finite-sized hard disks. They can collide with each other but have no long-range force among them. The algorithm is introduced in Section A2 in the Appendix. The system is scalable; an example unit system can be based on Å, fs, g/mol, and K.

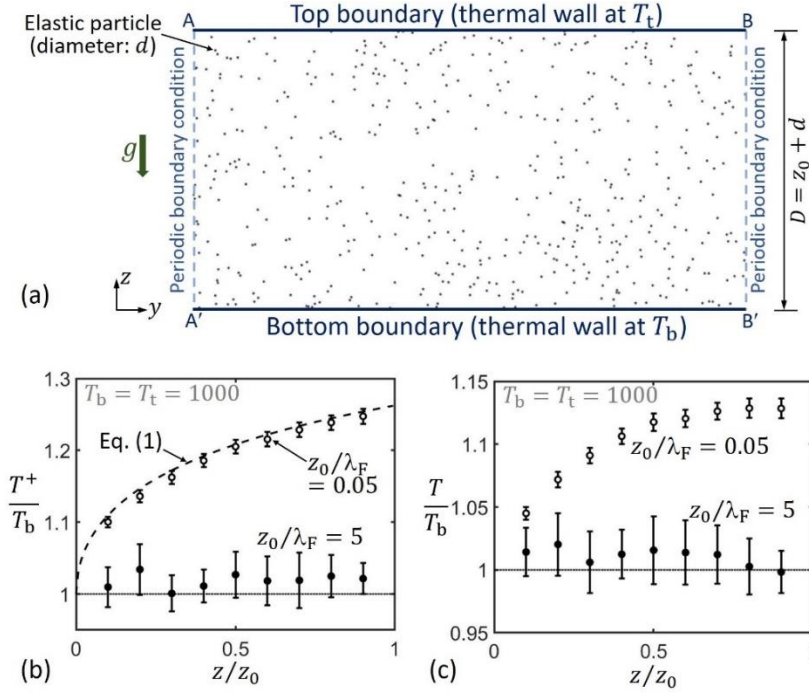


Figure 2 The energy-barrier model: (a) a 2D gas in a vertical plane in a uniform gravitational field (g). When the effective plane height ($z_0 = D - d$) is less than the nominal particle mean free path (λ_F), the system is a Knudsen gas and cannot reach thermal equilibrium. (b) Typical steady-state distribution of the kinetic temperature (T^+) along height z , for the ascending particles. The bottom wall and the top wall are at the same temperature ($T_b = T_t = 1000$). The dashed curve is calculated from Equation (1). In the chaotic case ($z_0/\lambda_F = 5$), T^+ is uniform along z , i.e., the system is at thermal equilibrium. In the nonchaotic case ($z_0/\lambda_F = 0.05$), T^+ is nonuniform along z , i.e., thermal equilibrium cannot be reached. (c) Typical steady-state distribution of the kinetic temperature for all the particles (T). The trend of the $T - z$ relationship is similar to that of T^+ in panel (b). The error bars represent the 95%-confidence interval.

The left and right borders (AA' and BB') are open and use periodic boundary condition. The upper and lower borders (AB and A'B') are thermal walls. Each thermal wall represents a large thermal reservoir. The top-wall temperature and the bottom-wall temperature are denoted by T_t and T_b , respectively. When a particle collides with a thermal wall, the reflected direction is random; the reflected speed is not correlated with the incident speed, but randomly follow the 2D Maxwell-Boltzmann distribution $p(v) = \beta m v \cdot e^{-\beta m v^2/2}$, where $\beta = 1/(k_B T_b)$ at the bottom boundary and $\beta = 1/(k_B T_t)$ at the top boundary. Such a thermal-wall boundary condition is commonly used in the study of rarefied gases [1,2]. A variety of different boundary conditions are examined in Figure 4 and Section 4.3 below, as well as [14]; the results demonstrate that the root cause of the intrinsically nonequilibrium steady state is not any specific form of boundary

condition, but the lack of extensive particle-particle collisions, i.e., nonchaoticity (also see Figure 3b,c).

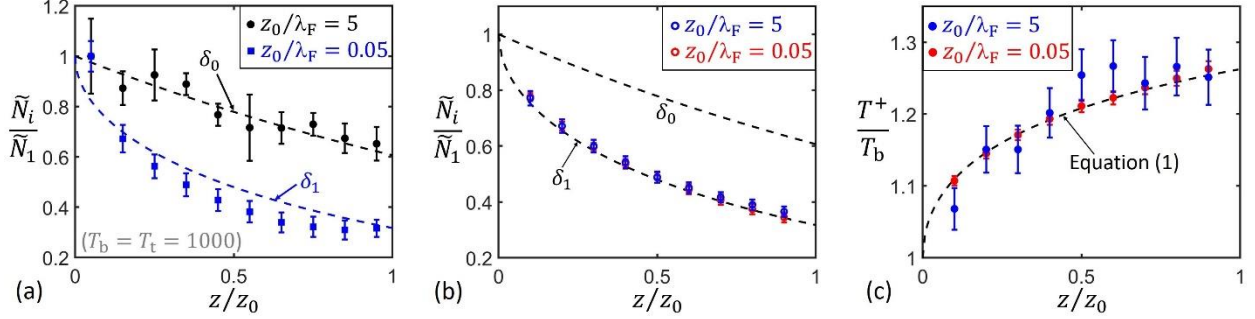


Figure 3. (a) The particle flux \tilde{N}_i , defined as the number of the particles crossing the lower border of the i -th horizontal layer in every 1000 timesteps. The top boundary and the bottom boundary are at the same temperature ($T_t = T_b = 1000$). The normalization factors (\tilde{N}_1) are 56.10 and 103.73 for $z_0/\lambda_F = 5$ and $z_0/\lambda_F = 0.05$, respectively. The error bars represent the 95%-confidence interval. When $z_0/\lambda_F = 5$, with extensive particle-particle collisions, \tilde{N}_i fits well with the Boltzmann factor $\delta_0 = e^{-\beta mgz}$. It reflects the behavior of a chaotic ideal gas. When particle-particle collisions are sparse ($z_0/\lambda_F = 0.05$), because the horizontal-dimension particle kinetic energy has little contribution to the vertical movement, fewer particles can overcome the gravitational energy barrier. Consequently, \tilde{N}_i is dominated by the z -component of particle velocity (v_z), and tends to follow $\delta_1 = \int_{\sqrt{2gz}}^{\infty} p_x(v_z) dv_z = 1 - \text{erf}(\sqrt{\beta mgz})$ [14], with $p_x = \sqrt{2\beta m/\pi} e^{-\beta m v_z^2/2}$ being the one-dimensional Maxwell-Boltzmann distribution of v_z . (b) The reference simulation for “ghost” particles: the steady-state \tilde{N}_i and (c) the steady-state T^+ as functions of height z . The particle-particle collision is turned off. All the other parameters and procedures are the same as in Figure 2 ($T_b = T_t = 1000$). The error bars represent the 95%-confidence interval. The red and the blue data points nearly overlap with each other, indicating that the particle-particle collision is the key factor.

The timestep is 0.01; the particle diameter $d = 1$; $m = 1$; $N = 500$. In all the simulation cases, $T_t = 1000$, and the total area of particle movement is $A_0 = w_0 z_0 = 39268.75$, where $z_0 = D - d$ is the effective plane height, and w_0 and D are the width and the height of the simulation box, respectively. The nominal particle mean free path is $\lambda_F = A_0/(\sqrt{8}Nd) \approx 27.77$. Initially, the particles are randomly distributed in the plane. Their speed follows the 2D Maxwell-Boltzmann distribution at T_b , and their direction is random.

The bottom-wall temperature (T_b) is set to be the same as T_t . The gas phase can be viewed as being immersed in a thermal bath. In different simulation cases, z_0 may be different, and g is adjusted accordingly to maintain a constant Boltzmann factor at the top wall $e^{-\beta mgz_0} = 0.607$. When $z_0 \gg \lambda_F$, the system represents a chaotic gas. When $z_0 \ll \lambda_F$, the system is a Knudsen gas

and, because the particle-particle collisions are rare, its performance is dominated by the particle-wall collisions at the upper and lower borders.

After the settlement period (10^5 timesteps), we monitor the velocity of every particle for two cases: $z_0/\lambda_F = 0.05$ and $z_0/\lambda_F = 5$. Along the vertical direction (z), the plane is virtually divided into 10 equal horizontal layers. Figure 2(b) shows typical steady-state profiles of the kinetic temperature of ascending particles, $T^+ = \bar{K}_i^+/k_B$, where \bar{K}_i^+ is the average kinetic energy of the particles moving upwards across the lower border of the i -th horizontal layer (from bottom to top, $i = 1, 2 \dots 10$). If both of the ascending and descending particles are considered, the overall temperature is given in Figure 2(c): $T = \bar{K}_i/k_B$, where \bar{K}_i is the average kinetic energy of all the particles crossing the lower border of the i -th horizontal layer.

Maxwell investigated the gravity effect on thermal equilibrium of a column of chaotic gas and concluded [25]: “...the temperature would be the same throughout (i.e., isothermal), or, in other words, gravity produces no effect in making the bottom of the column hotter or colder than the top.” This is visualized in Figure 2(b,c): when $z_0/\lambda_F = 5$, both T^+ and T tend to be homogeneous along z . It is consistent with Figure 3(a), where the particle flux distribution (\tilde{N}_i) for $z_0/\lambda_F = 5$ follows the Boltzmann factor. Figure 3(b,c) shows the reference tests on “ghost” particles. When the particle-particle collision is turned off, with everything else remaining the same as in Figure 2, regardless of z_0/λ_F , the steady-state distributions of \tilde{N}_i and T^+ are nonequilibrium, indicating that the dominant factor is the particle-particle collision.

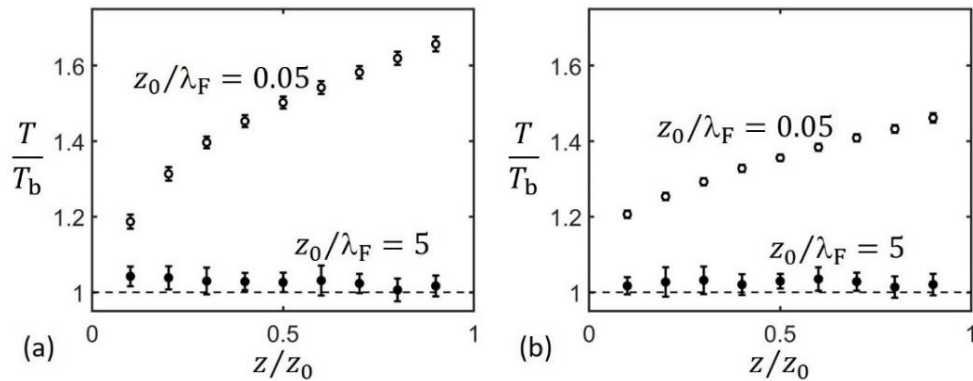


Figure 4. Effects of the boundary condition on the distribution of the gas-phase kinetic temperature (T). (a) Both of the bottom and the top boundaries are diffusive walls. The reflected particle direction is random; the reflected particle speed equals to the incident speed. (b) The bottom boundary is a thermal wall (the same as in Figure 2); the top boundary is a diffusive wall (the same as in panel (a)). All the other settings and procedures are the same as in Figure 2. The error bars represent the 95%-confidence interval.

When $z_0/\lambda_F = 0.05$, remarkably, the steady-state distributions of T^+ and T in Figure 2(b,c) are nonuniform, suggesting that without extensive particle-particle collision, there is no mechanism to drive the system to reach thermal equilibrium. Correspondingly, the steady-state distribution of \tilde{N}_i is non-Boltzmannian (see Figure 3a). As particle-particle collisions rarely happen, the gravity effect may be analyzed by using Liouville's theorem without the Boltzmann collision operator [14].

It is counterintuitive that T^+ and T increase with z . On the one hand, for every ascending or descending particle, the speed is higher at the bottom. On the other hand, while the high-energy particles may reach the top boundary, many more low-energy particles can only move around the bottom boundary. The two effects cannot counterbalance each other to render T independent of z ; otherwise, the steady-state particle distribution (i.e., the second law of thermodynamics) could be derived from the kinetic theory (i.e., Newton's second law). Overall, the average speed of the particles near the bottom is lower than near the top. The expected value of the kinetic energy of the ascending particles is $\bar{K}^+(z) = \bar{K}_y + \int_{mgz}^{\infty} (K_z - mgz) \cdot p_z(K_z) dK_z / \int_{mgz}^{\infty} p_z(K_z) dK_z$, where $\bar{K}_y = k_B T_b / 2$ is the average kinetic energy in the horizontal direction (y), and $p_z = e^{-\beta K_z} / \sqrt{\pi K_z k_B T_b}$ is the one-dimensional Maxwell-Boltzmann distribution of the z -dimension kinetic energy (K_z) at the bottom boundary ($z = 0$). Therefore,

$$T^+(z) = \frac{\bar{K}^+}{k_B} = \left[\frac{\Gamma(3/2, \beta mgz)}{\Gamma(1/2, \beta mgz)} - \frac{mgz}{k_B T_b} + \frac{1}{2} \right] T_b \quad (1)$$

where $\Gamma(x_1, x_2) = \int_{x_2}^{\infty} \xi^{x_1-1} e^{-\xi} d\xi$ is the upper incomplete gamma function. In Figure 2(c), the gradient of T is approximately a half of that of T^+ , which looks plausible, because T accounts for the descending particles, while T^+ does not. The result of T is in agreement with the previous simulation of a two-shelf system [14,15] (Section A3 in the Appendix). We tested different boundary conditions (Figure 4): as $z_0/\lambda_F \ll 1$, the $T - z$ gradient is always significant.

2.2 Spontaneous cold-to-hot heat transfer between a temperature difference

In Figure 5, T_b is varied, with everything else being the same as in Figure 2(b,c), with $z_0/\lambda_F = 0.05$. The ratio of T_b/T_t ranges from 0.6 to 1.0, the steady-state wall-to-gas heat-transfer rate is calculated as $\phi = \Sigma_r (K_r - K_i) / \Delta t$, where Σ_r indicates summation for all the particles

reflected by AB or A'B' in every $\Delta t = 2 \times 10^4$ timesteps. The reference rate is $\phi_0 = k_B T_t / t_0$, and the reference time $t_0 = z_0 \sqrt{m / (2k_B T_t)}$. Figure 6 shows typical time profiles of ϕ .

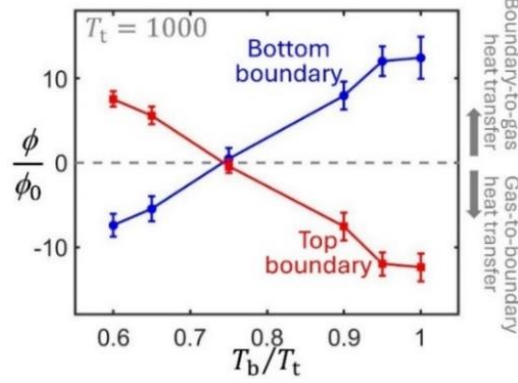


Figure 5. The steady-state wall-to-gas heat-transfer rates (ϕ) at the top boundary and the bottom boundary, as functions of T_b ($T_t = 1000$; $z_0/\lambda_F = 0.05$). The error bars indicate the 95%-confidence interval. When $T_b/T_t = 0.9$ or 0.95 , $\phi < 0$ at the top boundary and $\phi > 0$ at the bottom boundary; that is, without an energetic penalty, heat spontaneously transfers from the cold side (the bottom boundary) to the hot side (the top boundary) across the gas phase. When $T_b/T_t = 0.75$, $\phi \approx 0$ at both the top boundary and the bottom boundary; that is, effectively, the gas phase is thermally insulating.

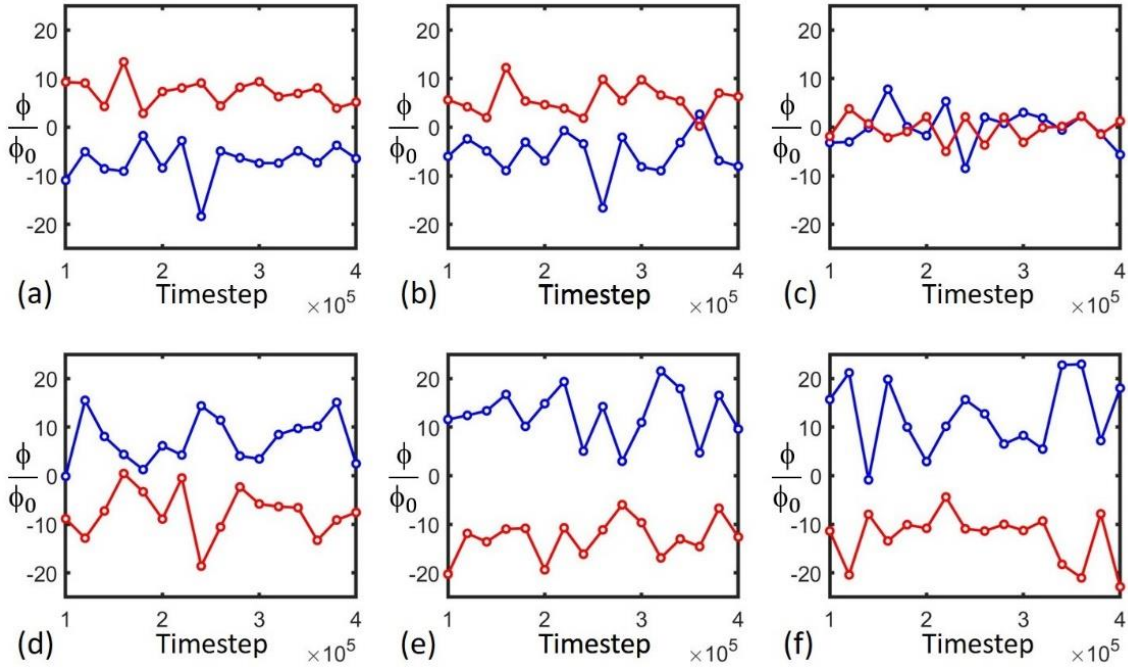


Figure 6. Typical time profiles of the wall-to-gas heat-transfer rates at the top thermal wall (the red lines) and the bottom thermal wall (the blue lines): (a) $T_b = 600$; (b) $T_b = 650$; (c) $T_b = 750$; (d) $T_b = 900$; (e) $T_b = 950$; (f) $T_b = 1000$. In all the simulation cases, $T_t = 1000$. In (d,e), heat transfers spontaneously from the bottom wall (the cold side) to the top wall (the hot side) across the gas phase. In (c), the heat flux is nearly zero, i.e., the gas phase is effectively thermally insulating.

When $T_b/T_t = 1$, the calculation reflects the nonequilibrium case in Figure 2(b,c). The heat influx at the top wall is dominated by T^+ . As T^+ increases with z , the top wall absorbs heat from the incident particles. The “extra” thermal energy comes from the heat desorbed by the bottom wall. When $T_b/T_t = 0.9$ or $T_b/T_t = 0.95$, the positive $T^+ - z$ gradient overcomes the negative $T_b - T_t$ difference, causing a continuous heat transport from the cold side (the bottom wall at T_b) to the hot side (the top wall at T_t). When $T_b/T_t = 0.75$, the effects of the $T^+ - z$ gradient and the $T_b - T_t$ temperature difference counterbalance each other. The overall heat flux is nearly zero and effectively, the gas phase is thermally insulating. Only when T_b is significantly lower than T_t ($T_b/T_t < 0.75$), can hot-to-cold heat transfer occur across the gas phase.

3. The second model: a switchable cell cluster of Knudsen gas

Section 2 analyzes heat transfer across a nonchaotic medium. It is also of interest to investigate heat transfer between a nonchaotic phase and a chaotic phase (e.g., a thermal wall). As discussed in the introductory section and detailed in Section A1 in the Appendix, at the steady state, the effective kinetic temperature of a Knudsen gas (T) is significantly less than the container-wall temperature (T_0), i.e., a Knudsen gas cannot relax to thermal equilibrium. Since $T < T_0$, the internal energy of the Knudsen gas (U) is lower than its equilibrium counterpart (U_0). Notice that thermodynamic equilibrium is an accessible state. If the Knudsen gas is initially at the equilibrium state (at T_0), as it evolves to the nonequilibrium steady state (at T), in accordance with the first law of thermodynamics, the reduction in U must be accompanied by a heat desorption (Q).

Figure 7(a) depicts a MC simulation of a 2D chaotic gas in a square container. Gravity is not considered. The container size (L) is 200; the particle number (N) is 500; the particle diameter (d) is 2; the particle mass (m) is 1; the timestep is 1. The particle mean free path is $\lambda_F = (L - d)^2 / (\sqrt{8}Nd) \approx 13.9$, much less than L . The effective gas-phase kinetic temperature is defined as $T = \bar{K}/k_B$. The boundaries are thermal walls at constant $T_0 = 100$. When a particle collides with a wall, the reflected direction is random; the reflected speed is not correlated with the incident speed, but randomly follow the 2D Maxwell-Boltzmann distribution of particle speed (v) at T_0 , $p_w(v) = \beta_0 m v \cdot e^{-\beta_0 m v^2/2}$, where $\beta_0 = 1/(k_B T_0)$. A variety of boundary conditions are tested in Section 4.3 below. The specific form of boundary condition does not affect whether

the system can reach thermal equilibrium; the critical mechanism of $T < T_0$ is nonchaoticity (i.e., $D < \lambda_F$).

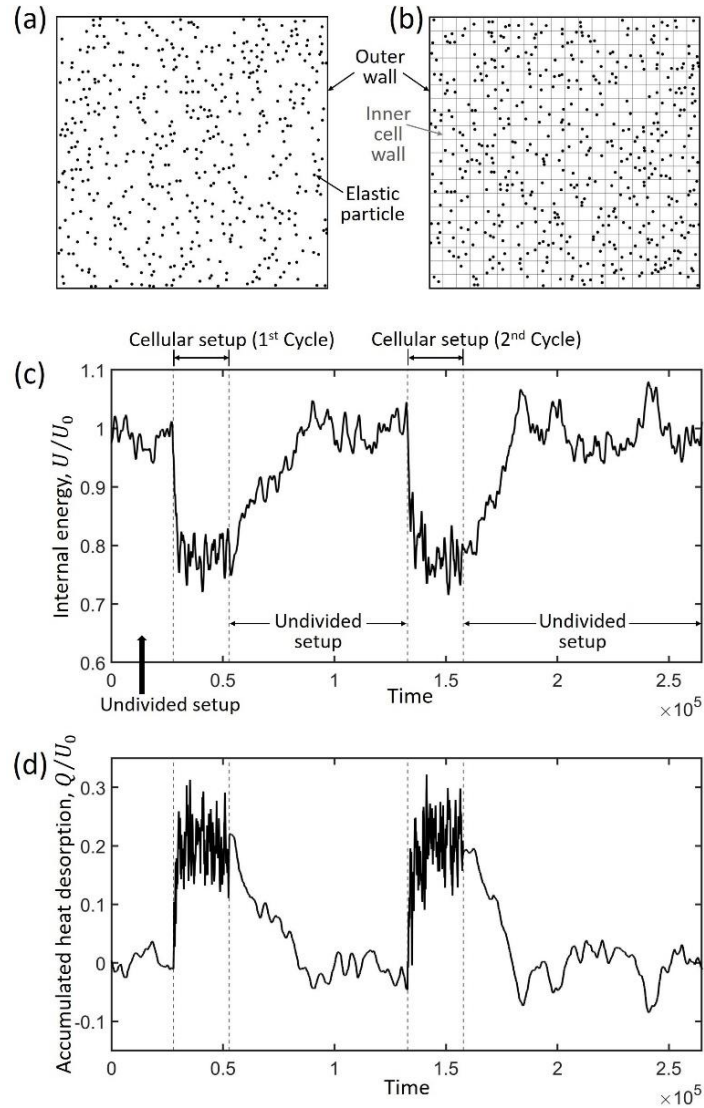


Figure 7 The time-dependent entropy-barrier model: **(a)** the undivided setup (a 2D chaotic gas), and **(b)** the cellular setup (each cell is a Knudsen gas). Gravity is not considered. The outer and inner boundaries are thermal walls at constant temperature T_0 . As the system shifts between the two configurations, the internal energy (U) changes, causing a significant heat flux through the walls. **(c)** A typical time profile of the internal energy (U) in two cycles of cell-wall insertion and removal ($U_0 = 0.029$). For each cycle, the first dashed vertical line indicates cell-wall insertion, and the second dashed vertical line indicates cell-wall removal. **(d)** The accumulated heat desorption across all the walls (Q), reported for every 100 particle-wall collisions. It matches the trend of U in panel (c).

After the settlement period (2×10^4 timesteps), at each timestep, the internal energy (U) is calculated as the total kinetic energy of all the particles, and the heat desorption (Q) as the

accumulated ΔK of all the particle-wall collisions, where $\Delta K = K_i - K_r$, and K_i and K_r are the incident and reflected particle kinetic energies, respectively. At the steady state, a set of divider walls are inserted, evenly separating the large container into 400 small cells (Figure 7b). The cell size ($D = 10$) is less than λ_F , so that each cell is a Knudsen gas. The inner cell walls use the same boundary condition as the outer walls. The simulation of the particle movement continues. At the new steady state, the cell walls are removed, and the simulation keeps running. After the system returns to the initial steady state, a second cycle of cell-wall insertion and removal is operated.

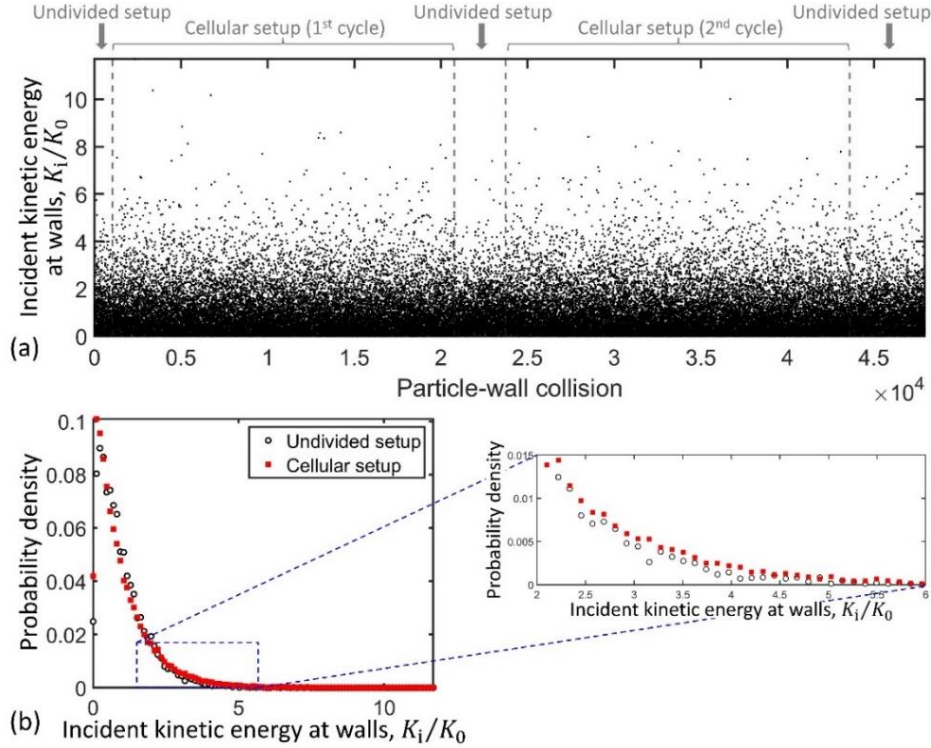


Figure 8 (a) The incident particle kinetic energy (K_i) at the container/cell walls, with $K_0 = k_B T_0$. Each data point represents a particle-wall collision. In the cellular setup, the particle-wall collisions happen more frequently than in the undivided setup. (b) The probability density of the distribution of K_i . The inset shows a magnified view for the high- K_i range. It can be seen that in the cellular setup, compared to the undivided setup, the probability density of the high- K_i particle-wall collisions ($K_i/K_0 \geq 2$) is consistently larger.

Figure 7(c) shows typical running average of U for every 1000 timesteps. When the system is changed from Figure 7(a) to Figure 7(b), the steady-state U decreases by about 20%, agreeing with the literature data [9,10]. The reduction in U (ΔU) is significant, but less than the ideal-case scenario of $T = T_0/2$ (Section A1 in the Appendix), which should be attributed to the occasional particle-particle collisions as well as the finite size of the simulation box. Corresponding to ΔU ,

about $0.2U_0$ heat is released from the gas phase into the thermal walls (Figure 7d). Figure 8 shows the distribution of the kinetic energy of incident particles (K_i). In the cellular setup, compared to the undivided setup, high-energy particle-wall collisions happen more frequently, which explains how, at the steady state, although $T < T_0$, the gas-wall heat exchange can be balanced. After the inner walls are removed, the system is converted back to the undivided state, and absorbs $\sim 0.2U_0$ heat from the environment. As the cell-wall insertion/removal is repeated, the heat desorption and absorption continue cyclically.

4. Discussion: time-dependent entropy barriers in a Knudsen gas (the second model)

4.1 Intrinsically nonequilibrium steady state

Figure 7(a) represents an ideal gas. It is a typical thermodynamic system and all its behaviors, including the inner cell walls in Figure 7(b), should be consistent with thermodynamic analysis. The cell walls block the particle movement and influence the probability of particle-particle collisions, and thus, may be viewed as entropy barriers. They are unrelated to Feynman's ratchet [26] or Maxwell's demon [27]. As discussed in [16], Feynman's ratchet is an equilibrium setup, having no nonchaotic component; mere geometrical asymmetry does not offer any nonequilibrium mechanism. Maxwell's demon is subject to the energetic penalty of information processing [28]. In Figure 7(a,b), on the contrary, the operation of the cell walls can be pre-programmed, without any knowledge of the specific position or momentum of each individual particle. Moreover, the heat flux in Figure 7(d) does not involve any random fluctuation or irreversible processes, e.g., the nonequilibrium paths associated with the Jarzynski equality [29].

In the cellular setup, the heat desorption spontaneously occurs from the "cold" gas phase ($T < T_0$) to the "hot" walls (at T_0). No matter how to define temperature, the heat exchange can be substantial and drive a heat engine to produce useful work by absorbing thermal energy from the environment without any other effects, contradicting the heat-engine statement of the second law of thermodynamics.

4.2 Basic principle of maximum entropy

4.2.1 Microcanonical ensemble

The intrinsically nonequilibrium steady state, although counterintuitive, is in line with the basic principle of maximum entropy [14,16]. It reassures us that the spontaneous heat flow does not contradict the fundamental logic of thermodynamics: the most probable state has the highest probability to be observed (measured by entropy).

Consider Figure 7(a,b) as an isolated system consisting of the gas phase and the environment (a thermal bath). For a microcanonical ensemble, the overall entropy is defined as

$$S = -k_B \sum_k \rho_k \ln \rho_k + S_E \quad (2)$$

where ρ_k is the probability of the k -th possible microstate of the gas phase, and $-k_B \sum_k \rho_k \ln \rho_k$ and S_E are entropies of the gas phase and the thermal bath, respectively.

The thermal bath is chaotic and is assumed to be at equilibrium. When the gas phase is also chaotic (Figure 7a), no detailed information is known about ρ_k , except for the following two constraints:

$$\sum_k \rho_k = 1 \quad (3)$$

$$\sum_k \rho_k \epsilon_k = U_g \quad (4)$$

where ϵ_k is energy of the k -th possible microstate of the gas phase, $U_g = U_S - U_E$ is the equilibrium gas-phase energy, U_S is the total system energy, and U_E is the thermal-bath energy. Equations (2-4) define the Lagrangian

$$\mathcal{L}_c = (-k_B \sum_k \rho_k \ln \rho_k + S_E) + \alpha_m (1 - \sum_k \rho_k) + \beta_m (U_g - \sum_k \rho_k \epsilon_k) \quad (5)$$

with α_m and β_m being the Lagrange multipliers. To maximize entropy (S),

$$\frac{\partial \mathcal{L}_c}{\partial \rho_k} = 0 \quad (6)$$

The solution of Equation (6) can be written as $\rho_k = e^{(-k_B + \delta_S - \alpha_m - \beta_m \epsilon_k)/k_B}$, where $\delta_S \triangleq \frac{\partial S_E}{\partial \rho_k} = C_S \delta_T$, $C_S = \frac{\partial S_E}{\partial T_0}$, and $\delta_T = \frac{\partial T_0}{\partial \rho_k}$. In accordance with Equation (4), $\delta_T = -\epsilon_k/C_E$, with C_E being the heat capacity of the thermal bath. Both C_E and C_S are properties of the thermal bath; they are nearly constant when the variation range of T_0 is narrow. Hence, $\rho_k \propto e^{-\beta_n \epsilon_k}$, with $\beta_n = (\beta_m + C_S/C_E)/k_B$. According to Equation (3),

$$\rho_k = \frac{1}{Z_e} e^{-\beta_n \epsilon_k} \quad (7)$$

where $Z_e = \sum_k e^{-\beta_n \epsilon_k}$. It fits with Boltzmann's assumption of equal *a priori* equilibrium probabilities. At thermal equilibrium, $\beta_n = \beta_0$. Substitution of Equation (7) into Equation (2) gives the maximum possible entropy (the global maximum) that the system can ever reach:

$$S_{\text{eq}} = S_E + k_B \ln Z_e + \frac{k_B}{Z_e} \sum_k \beta_n \epsilon_k e^{-\beta_n \epsilon_k} \quad (8)$$

Any other ρ_k (e.g., Equation 12 below) would result in a smaller entropy than S_{eq} , corresponding to a nonequilibrium state.

When the gas phase is formed by the nonchaotic Knudsen-gas cells (Figure 7b), the particle movements are less random than in the chaotic setup, i.e., more information of ρ_k is available. To derive analytical solutions, for the sake of simplicity, in this section, particle-particle collision is ignored. In the k -th possible microstate, for the l -th gas particle, denote its traveling distance and speed by \bar{x}_l and v_l , respectively; $t_l = \bar{x}_l/v_l$ is the retention time, i.e., the time duration between the previous and the next particle-wall collisions. Following the concept of $\rho_L \propto 1/v$ in the single-particle case in the introductory section, besides Equations (3,4), ρ_k is subject to an additional constraint $\rho_k \propto t_l$ (for all $l = 1, 2, \dots, N$), which may be formulated as

$$\rho_k = \xi_0 \prod_{l=1}^N \xi_l t_l \quad (9)$$

where ξ_0 is the normalization factor, and the coefficient of t_l (ξ_l) is a function of v_l . Since thermal equilibrium cannot be reached ($T < T_0$), $\xi_l t_l$ is not proportional to p_w , and Equation (9) is nontrivial. Equations (2-4 and 9) redefine the Lagrangian

$$\mathcal{L}_1 = \mathcal{L}_c + \sum_k \bar{B}_k \left(\rho_k - \xi_0 \prod_l \xi_l t_l \right) \quad (10)$$

where \bar{B}_k are the additional Lagrange multipliers. To maximize S , through

$$\frac{\partial \mathcal{L}_1}{\partial \rho_k} = 0 \quad (11)$$

we have

$$\rho_k = \frac{1}{Z_n} e^{B_k} e^{-\beta_n \epsilon_k} \quad (12)$$

where $Z_n = \sum_k e^{B_k} e^{-\beta_n \epsilon_k}$, and $B_k = \bar{B}_k/k_B$. Because of the nonchaoticity factor e^{B_k} and the thermally nonequilibrium steady state ($\beta_n \neq \beta_0$), Equation (12) is different from thermodynamic equilibrium (Equation 7). It is non-Boltzmannian and does not satisfy Boltzmann's assumption of equal *a priori* equilibrium probabilities. On the one hand, as the derivation is based on Equation

(11), entropy is maximized. Substitution of Equation (12) into Equation (2) gives the nonequilibrium entropy

$$S_{\text{ne}} = S_{\text{E}} + k_{\text{B}} \ln Z_{\text{n}} - \frac{k_{\text{B}}}{Z_{\text{n}}} \sum_k [(B_k - \beta_{\text{n}} \epsilon_k) e^{B_k} e^{-\beta_{\text{n}} \epsilon_k}] \quad (13)$$

On the other hand, the maximum possible entropy (i.e., the global maximum in the phase space) is associated with the equilibrium ρ_k in Equation (7), not the nonequilibrium ρ_k in Equation (12). Thus, $S_{\text{ne}} < S_{\text{eq}}$. The root cause of $S_{\text{ne}} < S_{\text{eq}}$ is that, compared to Equation (8), Equation (13) involves more restrictions on the maximization of entropy (Equation 9). In other words, S_{ne} is a local maximum in the phase space.

In order to account for the nonequilibrium steady state and comply with the basic principle of maximum entropy, the second law of thermodynamics may be generalized as follows [16]: in an isolated system, the difference between entropy (S) and the maximum possible steady-state entropy (S_{Q}) cannot increase, i.e.,

$$S \rightarrow S_{\text{Q}} \quad (14)$$

For a chaotic system, $S_{\text{Q}} = S_{\text{eq}}$, and Equation (14) is equivalent to the conventional entropy statement of the second law of thermodynamics. For a nonchaotic system, if $S_{\text{Q}} < S_{\text{eq}}$ and initially $S > S_{\text{Q}}$, entropy can decrease to S_{Q} without an energetic penalty. It is the fundamental mechanism behind the unusual thermal phenomena in Sections 2 and 3.

4.2.2 Canonical ensemble

Another perspective to analyze Figure 7(a,b) is to consider the gas phase as an isothermal system that is closed and immersed in the thermal bath. For a canonical ensemble, entropy of the gas phase is defined as

$$S = -k_{\text{B}} \sum_k \rho_k \ln \rho_k \quad (15)$$

When the gas phase is chaotic (Figure 7a), Equations (3,4,15) define the Lagrangian

$$\mathcal{L}_0 = -k_{\text{B}} \sum_k \rho_k \ln \rho_k + \alpha_k (1 - \sum_k \rho_k) + \beta_k (U_{\text{g}} - \sum_k \rho_k \epsilon_k) \quad (16)$$

where α_0 and β_k are the Lagrange multipliers. Maximization of S requires that

$$\frac{\partial \mathcal{L}_0}{\partial \rho_k} = 0 \quad (17)$$

The solution of Equations (17) and (3) is the Maxwell-Boltzmann distribution

$$\rho_k = \frac{1}{Z} e^{-\beta_0 \epsilon_k} \quad (18)$$

where $Z = \sum_k e^{-\beta_0 \epsilon_k}$ is the partition function, and $\beta_0 = \beta_k/k_B$. Equation (18) corresponds to thermodynamic equilibrium. Substitution of Equation (18) into Equation (15) gives the global maximum of entropy in the phase space

$$S_{\text{eq}} = k_B \ln Z + \frac{k_B}{Z} \sum_k \beta_0 \epsilon_k e^{-\beta_0 \epsilon_k} \quad (19)$$

When the gas phase is formed by the Knudsen-gas cells (Figure 7b), in addition to Equation (3), the nonchaotic particle movements provide more knowledge about the system microstates:

$$\rho_k \propto \prod_{l=1}^N p_w(v_l) \cdot t_l \quad (20)$$

Without defining the Lagrangian, combination of Equation (3) and Equation (20) determines ρ_k :

$$\rho_k = \mu_m \prod_{l=1}^N p_w(v_l) \cdot t_l \quad (21)$$

where μ_m is the normalization factor. Equation (21) is non-Boltzmannian and does not satisfy Boltzmann's assumption of equal *a priori* equilibrium probabilities. Substitution of Equation (21) into Equation (15) gives the nonequilibrium entropy

$$S_{\text{ne}} = -k_B \ln \mu_m - k_B \sum_k \left\{ \left[\mu_m \prod_{l=1}^N p_w(v_l) \cdot t_l \right] \cdot \sum_{l=1}^N \ln [p_w(v_l) \cdot t_l] \right\} \quad (22)$$

Because the thermal-wall boundary condition is governed by the Maxwell-Boltzmann distribution $p_w(v_l)$, S_{ne} represents the maximum entropy, but it is a local maximum in the phase space, smaller than the global maximum at thermodynamic equilibrium (Equation 19).

In Equations (18) and (21), T_0 is assumed constant. If the thermal bath is finite-sized, as the undivided setup (Figure 7a) is shifted to the cellular setup (Figure 7b), the heat desorption from the gas phase to the thermal bath would cause T_0 to rise slightly, accompanied by an entropy increase ΔS_c . However, ΔS_c occurs after the triggering event of the nonequilibrium state (the cell-wall insertion), independent of the spontaneous entropy reduction; it does not affect the final change of entropy, ΔS_0 (the difference between Equations 8 and 13). In the analysis of the isolated configuration in Section 4.2.1 (including both the gas phase and the thermal bath), the variation of the thermal-bath entropy $\left(\frac{\partial S_E}{\partial \rho_k}\right)$ is taken into account in the solution of Equation (6). As the system switches in between the cellular setup and the undivided setup, the overall entropy must decrease in one of the directions and increase in the other direction. Due to the additional constraint on ρ_k (Equation 9), entropy decrease happens from Figure 7(a) to Figure 7(b), without an energetic penalty. Even if ΔS_0 were somehow small despite the steady state in Figure 7(b) being

nonequilibrium, the heat flow (Q) could drive a heat engine to produce useful work in a cycle by absorbing heat from the thermal bath without any other effect.

4.3 The thermal-wall boundary condition

The thermally nonequilibrium steady state ($T < T_0$) does not rely on any specific characteristics of the boundary condition used in the computer simulation. In a numerical experiment, a variety of boundary conditions are tested for Figure 7(a,b). When a particle collides with a wall, the reflected direction is random, and the reflected speed (v_{re}) is determined through $v_{re}^2 = \alpha_{in}v_{in}^2 + (1 - \alpha_{in})v_{rd}^2$, where v_{in} is the incident speed, v_{rd} is a speed randomly generated from the 2D Maxwell-Boltzmann distribution at T_0 , and α_{in} represents the “memory” of the particle-wall interaction. In different simulations, α_{in} is varied from 0 to 1/2. When $\alpha_{in} = 0$, v_{re} is reduced to the ideal thermal-wall condition in Section 3; when $\alpha_{in} > 0$, the degree of randomness of the particle-wall collision is lower. The results show that in the range of α_{in} under investigation, it has no statistically significant influence on the steady state. It does affect the rate of convergence. With a larger α_{in} , the system tends to take more time to reach the steady state, and vice versa.

In another numerical experiment on the cellular setup, α_{in} is set to 1 (i.e., $v_{re} = v_{in}$). The reflected angle is either random (diffuse reflection) or equal to the angle of incidence (specular reflection). In both cases, the system is isolated, and the internal energy does not vary. The average kinetic energy of the incident particles is significantly higher by ~20% than the average kinetic energy of all the particles in the gas phase.

In yet another numerical experiment on the undivided setup, particle-particle collision is turned off. The particle-wall collision is not affected ($\alpha_{in} = 0$). At the container walls, a significant heat desorption is observed, similar to the heat exchange at the cell walls in the cellular setup. It confirms that the lack of extensive particle-particle collisions is the key factor of the spontaneously nonequilibrium system behavior.

The thermal-wall boundary condition reflects the basic concept of path independence of thermodynamics. It represents the effects of a chaotic body (the thermal bath) and has no nonequilibrium mechanism, i.e., it cannot be responsible for the nonequilibrium phenomena. To further understand the ideal case of $\alpha_{in} = 0$, we may assume that the cell walls are covered by a

layer of perfect heat exchangers. During a particle-wall interaction event, the particle fully exchanges kinetic energy with the environment through the heat exchangers, before it eventually departs back into the gas phase.

5. Discussion: Knudsen gas in gravity (the first model)

5.1 Intrinsically nonequilibrium steady-state temperature distribution

According to Figures 2 and 5, the nonchaotic system cannot reach thermal equilibrium. At the steady state, when $T_b = T_t$ (i.e., the Knudsen gas is immersed in a thermal bath), not only is the temperature distribution nonuniform, but also the heat exchange at the upper/lower boundaries (Q) is significant. When $T_b/T_t = 0.75$, $Q \approx 0$, i.e., the gas phase is effectively thermally insulating, despite the significant difference between T_b and T_t . When $0.75 < T_b/T_t < 1$, the cold-to-hot heat transfer is spontaneous, incompatible with the refrigeration statement of the second law of thermodynamics. Moreover, because the $T - z$ gradient is dependent on the gravitational energy barrier (mgz_0), two different gases can form Maxwell's double-column engine (see Section A4 in the Appendix [30]), which continuously produces useful work by absorbing heat from the environment, as depicted in Figure 9. It is inconsistent with the heat-engine statement of the second law of thermodynamics.

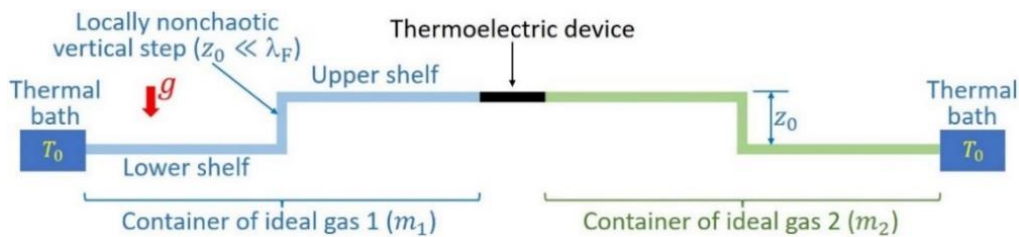


Figure 9. An example of Maxwell's double-column engine [30]. Two identical containers contain different ideal gases, in a uniform gravitational field (g). The gas-particle masses in the two containers are m_1 and m_2 , respectively. Each container consists of an upper shelf and a lower shelf, with the height difference (z_0) much less than the nominal mean free path of the gas particles (λ_F). The lower shelves of the two containers are in contact with the same thermal bath at temperature T_0 . A thermoelectric device is sandwiched in between the two upper shelves. As the temperature field is nonuniform along the vertical direction, because $m_1 \neq m_2$, the effective gas-phase temperatures at the two upper shelves are different. Thus, the thermoelectric device can continuously produce useful work by absorbing heat from the thermal bath, without any other effect.

There are a few points worth noting. Firstly, in Figure 5, the heat desorption of the gas particles at the upper boundary is balanced by the heat absorption at the lower boundary, obeying the first law of thermodynamics. Secondly, the system does not consume energy from the gravitational field. At the steady state, on average, for every ascending particle, there is a descending particle; vice versa. Thirdly, Figure 2(a) is fundamentally different from Earth's atmosphere. In [31], Maxwell stated: "In the case of the atmosphere, the effect of wind is to cause the temperature to vary as that of a mass of air would do if it were carried vertically upwards, expanding and cooling as it ascends." Earth's atmosphere is exposed to the ground and outer space, resulting in the macroscopic convection of air. As air rises, it undergoes adiabatic expansion and tends to be colder at the top. On the contrary, in Figure 2(a), as $T_b = T_t$, the system is immersed in a thermal bath, and there is no planar Fourier flow. Even if the gas could rise, without extensive particle-particle collisions, the increase in volume cannot do work, similar to free expansion in vacuum. That is, the Knudsen gas has no mechanism to render the top section cooler. In fact, in Figure 2(b,c), T is higher at the top.

5.2 The basic principle of maximum entropy

For the k -th possible microstate of the gas phase, use K_l , v_{zl} and z_l to denote the kinetic energy, the z -component of velocity, and the height of the l -th gas particle, respectively. In Figure 2, the nonchaotic particle movement imposes additional constraints on ρ_k . Somewhat similar to Equation (20), if particle-particle collision is ignored,

$$\rho_k = \mu_n \bar{r}_k \tilde{r}_k \quad (23)$$

where μ_n is the normalization factor determined by Equation (3); $\bar{r}_k = \prod_{l=1}^{N_b} p_z(K_{1l}) \cdot t_{al}$ and $\tilde{r}_k = \prod_{l=1}^{N_t} p_t(K_{2l}) \cdot t_{dl}$ represent the contributions of the particles reflected into the vertical plane from the bottom boundary and the top boundary, respectively; N_b and N_t are the numbers of the particles from the bottom boundary and the top boundary, respectively; p_z and p_t are the one-dimensional Maxwell-Boltzmann distribution functions of kinetic energy at T_b and T_t , respectively; $K_{1l} = K_l + mgz_l$ and $K_{2l} = K_l - mgz_l$ are the initial kinetic energy of the l -th particle, immediately after the previous particle-wall collision; t_{al} and t_{dl} are the time duration between the previous and the next particle-wall collisions. For the particles from the bottom

boundary, the initial z -component of velocity is $v_{1l} = \sqrt{v_{zl}^2 + 2gz_l}$. If $v_{1l} < \sqrt{2gz_0}$, $t_{al} = 2v_{1l}/g$; if $v_{1l} \geq \sqrt{2gz_0}$, $t_{al} = (v_{1l} - \sqrt{v_{1l}^2 - 2gz_0})/g$. For the particles from the top boundary, the initial z -component of velocity is $v_{2l} = \sqrt{v_{zl}^2 - 2gz_l}$, and $t_{dl} = (\sqrt{v_{2l}^2 + 2gz_0} - v_{2l})/g$.

Substitution of Equation (23) into Equation (15) gives the nonequilibrium entropy

$$S_{ne} = k_B \ln \mu_n - k_B \mu_n \sum_k (\bar{r}_k \tilde{r}_k \ln \bar{r}_k \tilde{r}_k) \quad (24)$$

As the thermal-wall boundary condition is governed by the Maxwell-Boltzmann distribution (p_z and p_t), Equation (24) represents the maximum entropy. Similar to the discussion in Section 4.2, because of the nonchaoticity constraints on ρ_k , S_{ne} is a local maximum in the phase space, less than its chaotic counterpart.

6. Discussion: considerations on experimental realization

The non-thermodynamic phenomena in Sections 2 have never been reported for real-world systems, which should be attributed to the weak gravitational field of Earth ($\beta mgz_0 \approx 10^{-12}$ for air molecules). It would be interesting to explore whether, in a high- g environment, the effects of nonchaoticity can be nontrivial, and whether the concept can be demonstrated by a stronger thermodynamic force, such as the Coulomb force. Notice that if a conductive or semiconductive nanolayer is placed in an electric field, the screening effect must be taken into consideration, e.g., by keeping the characteristic size smaller than the Debye length or the spacing of the charge carriers. Cooper pairs could have unique properties.

Section 3 circumvents the hurdle of the large energy barrier. However, the idealized process of cell-wall insertion/removal may be difficult to achieve, because gas transport is influenced by surface adsorption [32]. This difficulty may be resolved by using a setup consisting of two identical chambers. One set of divider walls are alternately inserted and removed between the two chambers. Thus, the adsorbed gas particles on the cell walls only have internal effects.

Interestingly, in a study on nonwetting liquids in nanopores [33,34], there may have already been experimental evidence of the effects of time-dependent entropy barriers. In [34] (Figure 10a), 1 g nanoporous silica particles were immersed in 5 g nonwetting liquid, sealed in a steel container with a thermal insulation layer. A pressure (P) was maintained on the liquid phase through the piston, so that the liquid was forced to fill the nanopores. Then, P was gradually reduced,

accompanied by liquid defiltration. The temperature of the bulk liquid phase was monitored by the embedded sensor. Thermodynamic analysis suggests that separation of a liquid from a hydrophobic solid surface has the tendency to cause a temperature increase, not a temperature decrease. However, a large reduction in temperature ($\Delta T_s \approx -1.5 \text{ }^\circ\text{C}$) was measured (Figure 10b). Such a ΔT_s corresponds to a loss of thermal energy $U_L \approx 30 \text{ J}$, while the total work done by the piston (E_P) is only about 16 J. Even if cooling could happen and E_P were fully utilized for cooling with 100% efficiency, $|\Delta T_s|$ should not exceed $0.7 \text{ }^\circ\text{C}$. These unusual phenomena may be attributed to the “Knudsen gas like” characteristics of the confined liquid. As the pore size is comparable with the mean free path of the liquid molecules, the kinetic temperature of the confined liquid is less than the nanopore-wall temperature. Thus, when the confined liquid molecules move out of the nanopores, the overall temperature becomes lower. Similarly, liquid infiltration resulted in a large temperature increase $\Delta T_s \approx +2.1 \text{ }^\circ\text{C}$; the associated gain of thermal energy ($U_G \approx 44 \text{ J}$) was significantly greater than E_P . The difference between U_G and U_L was close to E_P , in agreement with that E_P was mostly dissipated through hysteresis. Figure 10(c) illustrates a design of circular flow, wherein the steady-state liquid-solid interaction does not vary over time. The resistance to the movement of the nonwetting liquid tends to be low, thanks to the superfluidity effect in nanoenvironment [35-37].

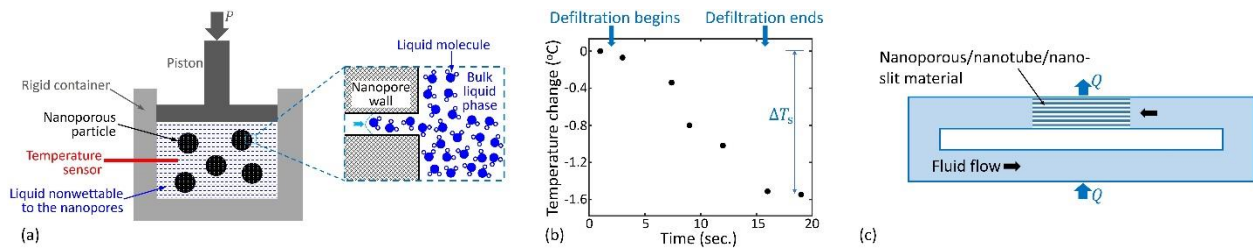


Figure 10. (a) The experimental setup in [33,34]. The temperature variation associated with liquid defiltration from the nanoporous particles is measured. (b) Typical testing data of temperature change (ΔT_s) [34]: temperature considerably decreases when the nonwetting liquid defiltrates out of the nanoporous silica. (c) Schematic of a nanofluidic setup of continuous flow, based on the same concept as in panel (a). The system is closed and immersed in a thermal bath. The effective nanochannel size is smaller than or comparable with the mean free path of the fluid particles. As the fluid enters the nanochannels, it releases heat (Q) to the environment, because of the nonequilibrium effect. Likewise, when the fluid comes out of the nanochannels, it absorbs heat from the environment.

To apply the concept of time-dependent entropy barriers to the charge carriers in a mesoscopic physical system, “cell walls” may be formed by using adjustable potential wells,

outer/inner boundaries, asymmetric scattering or reflection, etc. The upper limit of the power density could be more than 10^4 kW/cm³ (Section A5 in the Appendix). Multiple units can be connected in parallel or in tandem, to amplify the temperature difference and the heat flux.

7. Concluding remarks

It has long been known that certain nonchaotic particle movements cannot be analyzed by thermodynamics; usually, their energy properties are considered “trivial.” In current research, we demonstrate that beyond the boundaries of Boltzmann’s H-theorem, there are non-thermodynamic systems with nontrivial heat transfer properties. One example is the Knudsen gas in gravity (Figure 2), and the other example is the switchable Knudsen-gas cell cluster (Figure 7). In both cases, without any other effect, heat can spontaneously transfer from the cold side to the hot side, allowing for production of useful work by absorbing heat from a single thermal reservoir. Such counterintuitive phenomena are incompatible with the conventional refrigeration statement and heat-engine statement of the second law of thermodynamics. They are rooted in the intrinsically nonequilibrium steady state, in line with the basic principle of maximum entropy.

Appendix

A1. Knudsen gas: intrinsically nonequilibrium steady state

The numerical simulations in Sections 2 and 3 take into account the particle-particle collisions. The particles collide with each other whenever they meet. However, in a Knudsen gas, compared to the particle-wall collisions, because the particle-particle collisions are sparse, their effect is secondary. In this section, for the sake of simplicity, to obtain analytical solutions, particle-particle collision is ignored. Such a simplification may be realized in Figure 7(b): in the cellular setup, if the number of the cells is much larger than the number of the particles, the system state is dominated by the cells that each contains only one particle. The few crowded cells remain chaotic and do not contribute to the heat exchange. The empty cells are also trivial. In a single-particle cell, it is impossible for the particle to encounter another particle, and the effective mean free path of particle-particle collision $\lambda_F \rightarrow \infty$. The mean free path of particle-wall collision is $\lambda_w = \pi D/4$ [12], with D being the cell size. Hence, $\lambda_F \gg \lambda_w$.

Figure 11(a) depicts a Knudsen-gas cell, with the cell boundaries being made of thermal walls. The reflected particle speed (v) follows the 2D Maxwell-Boltzmann distribution $p_w(v) = \beta_0 m v \cdot e^{-\beta_0 m v^2/2}$, where $\beta_0 = 1/(k_B T_0)$, k_B is the Boltzmann constant, T_0 is the cell-wall temperature, and m is the particle mass. The reflected particle direction is random. Use $\rho_L(v)$ to denote the probability density of finding the particle at speed v . Without particle-particle collision, ρ_L is proportional to the retention time λ_w/v , i.e., the average time duration between two consecutive particle-wall collisions. Therefore, $\rho_L(v) \propto p_w(v)/v$, and its normalized form is

$$\rho_L = \sqrt{\frac{2\beta_0 m}{\pi}} e^{-\beta_0 m v^2/2} \quad (\text{A1})$$

Figure 11(b) compares $\rho_L(v)$ to $p_w(v)$. The average particle speed of ρ_L is lower than that of $p_w(v)$, as it should be. Since the time interval between particle-wall collisions is inversely proportional to the particle speed (v), it is more likely to find a slow particle than a fast particle in the cell. No reasonable boundary condition could keep the confined particle at thermal equilibrium, i.e., the time-average particle kinetic energy (\bar{K}) cannot be equal to $k_B T_0$. For a single-particle cell, according to Liouville's theorem [3], at the steady state

$$0 = v_x \frac{\partial \rho_L}{\partial x} + v_y \frac{\partial \rho_L}{\partial y} \quad (\text{A2})$$

where x and y are the coordinates of the particle, and v_x and v_y are the x- and y-components of particle velocity (\vec{v}), respectively. Its general solution is $\rho_L = f_L(\vec{v})$, where f_L may be any differentiable function. Because the system is isotropic,

$$\rho_L = f_L(v) \quad (\text{A3})$$

The Maxwell-Boltzmann distribution $p_w(v)$ is just one special case of $f_L(v)$. Without chaotic particle-particle collisions, the Bhatnagar-Gross-Krook (BGK) operator of the Boltzmann equation is irrelevant and there is no mechanism to ensure $\rho_L = p_w(v)$. At the intrinsically nonequilibrium steady state ($\rho_L \propto p_w/v$ in Equation A1), the effective gas-phase temperature is

$$T = \frac{1}{k_B} \int_0^\infty \frac{mv^2}{2} \rho_L dv = \frac{1}{k_B} \int_0^\infty \left[\frac{mv^2}{2} \left(\sqrt{\frac{2\beta_0 m}{\pi}} e^{-\beta_0 mv^2/2} \right) \right] dv = \frac{T_0}{2} \quad (\text{A4})$$

In the numerical simulation in Figure 7, T is significantly less than T_0 , but because of the occasional particle-particle collisions, it is larger than the ideal-case scenario of $T_0/2$.

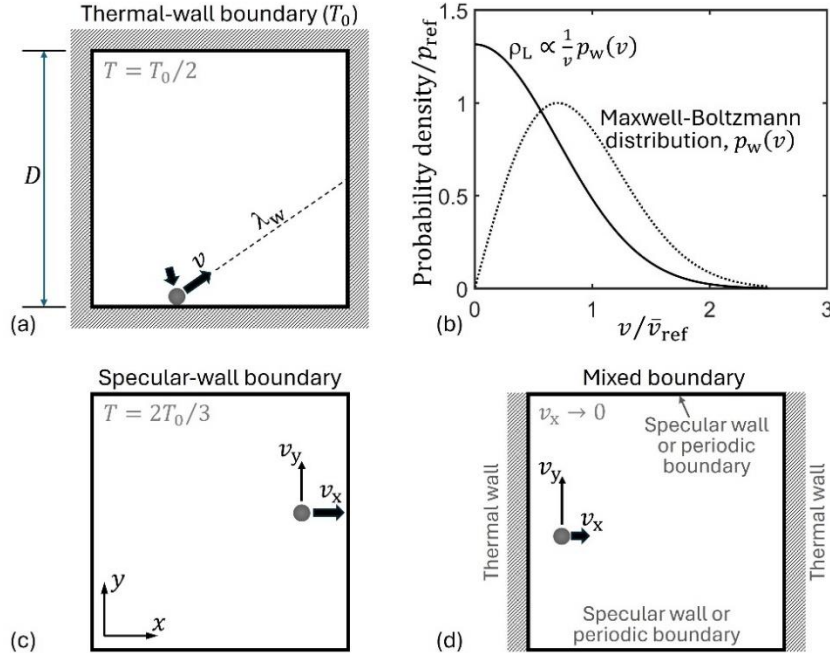


Figure 11. Three Knudsen-gas models that exhibit thermally nonequilibrium steady states. **(a)** A Knudsen-gas cell, with the cell boundaries being made of thermal walls. The wall temperature is constant T_0 ; $\lambda_w = \pi D/4$ indicates the average traveling distance of the particle between two consecutive particle-wall collisions. At the steady state, the effective gas-phase temperature $T = T_0/2$. **(b)** Comparison between $p_w(v)$ and $\rho_L \propto p_w(v)/v$, as functions of the particle speed (v). The normalization factor (p_{ref}) is the peak value of $p_w(v)$, and $\bar{v}_{\text{ref}} = \sqrt{2k_B T_0/m}$. **(c)** A Knudsen-gas cell, with the boundaries being made of specular walls. The particle movements in the x and y directions are uncorrelated. At the steady date, $T = 2T_0/3$. **(d)** A Knudsen-gas cell. The two cell borders normal to the x axis are thermal walls; the cell borders normal to the y axis are specular walls or use periodic boundary condition. At the steady state, $v_x \rightarrow 0$.

In comparison, in a chaotic gas (e.g., a large body of classical ideal gas), due to the random particle-particle collisions, $\rho_L \propto p_w(v)/v$ is inapplicable. No particle can reach the boundary without interacting with other particles. In a short time period \bar{t}_0 , the particle influx at boundary (i.e., the number of particle-wall collisions per unit boundary length) can be calculated through the mean-field theory: $\bar{N}_n = \rho_0(\bar{v}_x\bar{t}_0)/2$, where ρ_0 is the particle number density, and \bar{v}_x is the average component of incident velocity normal to the boundary. The average kinetic energy of the incident particles is

$$\bar{K}_{\text{in}} = \frac{1}{\bar{N}_n} \left[\bar{N}_n \int_0^\infty \frac{mv^2}{2} (\beta_T m v \cdot e^{-\beta_T m v^2/2}) dv \right] = k_B T \quad (\text{A5})$$

where $\beta_T = 1/(k_B T)$. Consequently, at the steady state,

$$T = \frac{\bar{K}_{\text{in}}}{k_B} = T_0 \quad (\text{A6})$$

That is, thermal equilibrium is reached.

In general, for a nonchaotic gas, depending on the boundary condition and initial condition, f_L may be in various forms. Figure 11(c) shows a Knudsen-gas cell formed by specular walls. The particle movements in the x- and y-directions are independent of each other. Consider an initial condition where the particle speed follows the Maxwell-Boltzmann distribution. In a short time period \bar{t}_0 , the effective particle influx at boundary is not \bar{N}_n , but $\bar{N}_c = \frac{1}{2} \int_0^\infty [\rho_0 v_x \bar{t}_0 p_x(v_x)] dv_x$, where v_x indicates the component of incident velocity normal to the boundary, and $p_x = \sqrt{2\beta_T m/\pi} e^{-\beta_T m v_x^2/2}$ is the one-dimensional Maxwell-Boltzmann distribution function of $|v_x|$. At the cell wall, the average kinetic energy of the incident particles is

$$\bar{K}_{\text{in}} = \frac{1}{\bar{N}_c} \left\{ \frac{1}{2} \int_0^\infty \frac{mv_x^2}{2} [\rho_0 v_x \bar{t}_0 p_x(v_x)] dv_x \right\} + \bar{K}_{\text{pr}} = \frac{3}{2} k_B T \quad (\text{A7})$$

where $\bar{K}_{\text{pr}} = k_B T/2$ is the average particle kinetic energy in the dimension parallel to the boundary. Hence, at the steady state,

$$T = \frac{2\bar{K}_{\text{in}}}{3k_B} = \frac{2}{3} T_0 \quad (\text{A8})$$

which is not at thermal equilibrium (i.e., $T \neq T_0$). A key difference between Equation (A8) and Equation (A4) is whether the steady-state distribution of the particle speed (v) is Boltzmannian.

Figure 11(d) depicts another model that cannot relax to thermal equilibrium. The two cell borders normal to the x axis are thermal walls. The two borders normal to the y axis either use

periodic boundary condition or are specular walls. The particle movement in the y direction does not affect v_x . Under this condition, if particle-particle collision is ignored, the calculated steady-state v_x would be near-zero, because $\int_0^\infty v_x^{-1} p_x dv_x \rightarrow \infty$. It may be understood as follows: in an ensemble of the cells, the gas particles of the lowest v_x tend to remain in the interior, while the high- v_x particles randomly change their velocities upon colliding with the thermal walls. Eventually, every particle tends to have an arbitrarily small v_x , since it takes a nearly infinitely long time for such a particle to travel across the cell to collide with a thermal wall again.

It is worth noting that chaoticity may not explicitly affect the calculation of pressure. In a chaotic gas, at the container wall, the pressure can be obtained as

$$\bar{P}_{\text{wall}} = \frac{1}{\bar{t}_0} \int_0^\infty \int_0^{\pi/2} (2mv \cos \theta) \cdot \bar{N}_n(\beta_T mv \cdot e^{-\beta_T mv^2/2}) d\theta dv = \rho_0 k_B T \quad (\text{A9})$$

with θ being the incident angle. It is the ideal-gas law, as expected. In the Knudsen-gas model of Figure 11(c), without particle-particle collision, the gas pressure is

$$P_{\text{wall}} = \frac{1}{\bar{t}_0} \frac{1}{2} \int_0^\infty (2mv_x) (\rho_0 v_x \bar{t}_0) p_x dv_x = \rho_0 k_B T \quad (\text{A10})$$

which is also the ideal-gas law. Compared to the chaotic gas, the difference in particle influx of the Knudsen gas is offset by the variation in cell-wall temperature.

It is also worth noting that in a three-dimensional (3D) space, Figure 11(d) represents a setup with confinement in one dimension, e.g., a slit between two solid layers; Figure 11(a) represents a setup with confinement in two dimensions, e.g., a tube or a pore. If the setup is confined by thermal walls in all the three dimensions (e.g., a hollow cell), $p_w(v)$ should be the 3D Maxwell-Boltzmann distribution function at T_0 , and $\rho_L \propto p_w/v$ can be normalized as $\rho_L(v) = m\beta_0 v \cdot e^{-\beta_0 mv^2/2}$. The effective gas-phase kinetic temperature is

$$T = \frac{2}{3k_B} \int_0^\infty \frac{mv^2}{2} \rho_L(v) dv = \frac{2}{3} T_0 \quad (\text{A11})$$

In fact, if Figure 11(a,d) are considered as 3D cases, as the unconfined dimensions are taken into account, $T = 2T_0/3$ generally holds true. It is consistent with Figure 11(c) wherein the particle movements in different dimensions are uncorrelated with each other.

A2. Algorithm of the computer programs

The computer programs used in the current investigation are available at [17]. In the 2D system, the particles are billiard-like finite-sized hard disks. The particle-particle and particle-wall

collisions happen in the middle of the timesteps. In each timestep, the program first computes the virtual position of every particle at the end of the timestep, as if particle collision could not happen. Then, collision is identified as the particle-particle or particle-wall overlapping. The exact collision location and time are calculated by tracing the particle trajectories, and the correct particle information is updated by solving Newton's equations (conservation of energy and momentum). Finally, the next timestep begins. The time resolution is high, so that the expected value of the particle displacement in a timestep is less than 5% of the particle size. The probability of missing a collision is practically zero (less than 10^{-170}).

In Section 3, the cell-wall insertion or removal does not take time. During a cell-wall insertion, if a particle overlaps with a cell wall, the particle would be moved away from the wall by one particle radius, with everything else being unchanged. If this operation causes conflict with another particle, the simulation case would be abandoned.

A3. Consistency with the two-shelf system

In [15], Monte Carlo simulations are performed on a two-shelf system. The system consists of two shelves at different heights in a uniform gravitational field (g), connected through a vertical step. A large number of two-dimensional elastic particles (hard disks) randomly move on the two shelves across the vertical step. The shelf size is large, so that the particle movement in the shelves is ergodic and chaotic. The height difference between the two shelves (z_0) is much less than the nominal particle mean free path (λ_F), so that the particle transmission across the step tends to be locally nonchaotic. Compared with Figure 2(a), the step is analogous to the vertical plane, and the chaotic gases in the two shelves are the counterparts of the thermal walls.

When $\beta_0 mgz_0 = 0.5$, it was observed that at the steady state, the average particle speed on the upper shelf was larger than on the lower shelf by $10.4 \pm 1.3\%$, with the data range indicating the 90%-confidence interval. Moreover, the particle number density ratio between the upper shelf and the lower shelf is significantly less than the Boltzmann factor, consistent with the lower curve in Figure 3(a).

A4. Maxwell's double-column engine

In [26], for the effect of gravity on thermal equilibrium, Maxwell pointed out: "...if the temperature of any substance, when in thermic equilibrium, is a function of the height, that of any other substance must be the same function of the height. For if not, let equal columns of the two substances be enclosed in cylinders impermeable to heat, and put in thermal communication at the bottom. If, when in thermal equilibrium, the tops of the two columns are at different temperatures, an engine might be worked by taking heat from the hotter and giving it up to the cooler, and the refuse heat would circulate round the system till it was all converted into mechanical energy, which is a contradiction to the second law of thermodynamics. The result as now given is, that temperature in gases, when in thermal equilibrium, is independent of height, and it follows from what has been said that temperature is independent of height in all other substances."

A5. Assessment of power density

For the sake of simplicity and to be conservative, in a metal, we only consider the high-energy conduction electrons that approximately follow the Maxwell-Boltzmann distribution. Their number density is on the scale of 10^{20} cm^{-3} and the Fermi energy is a few eV, leading to an energy density on the scale of 10^7 J/m^3 . In Figure 7(d), the heat desorption is ~20% of the internal energy. If this ratio is also relevant to the charge carriers, with the duration of each operation cycle being $0.1 \text{ } \mu\text{s}$, the upper limit of the power density may be more than 10^4 kW/cm^3 .

References

1. M. N. Kogan. *Rarefied Gas Dynamics*. New York: Springer (1969).
2. J. R. Dorfman. *An Introduction to Chaos in Nonequilibrium Statistical Mechanics* (Cambridge University Press, Cambridge, 1999).
3. M. Kardar. *Statistical Physics of Particles* (Cambridge Univ. Press, 2007), p. 74.
4. A. S. Kannan, T. S. B. Narahari, Y. Bharadhwaj, A. Mark, G. Sardina, D. Maggiolo, S. Sasic, H. Ström. The Knudsen paradox in micro-channel Poiseuille flows with a symmetric particle. *Appl. Sci.*, **11**, 351 (2021)
5. Z. Ulker, D. Sanli, C. Erkey. Applications of aerogels and their composites in energy-related technologies. In: V. Anikeev, M. Fan (ed.), *Supercritical Fluid Technology for Energy and Environmental Applications*, Elsevier (2014).
6. A. Kawabata. Ballistic electron transport. In: T. Ando, Y. Arakawa, K. Furuya, S. Komiyama, H. Nakashima (ed.), *Mesoscopic physics and electronics* (Springer, 1998)
7. G. Lebon, D. Jou. *Understanding Nonequilibrium Thermodynamics*, Springer, 2008
8. J. R. Dorfman. *An Introduction to Chaos in Nonequilibrium Statistical Mechanics*, Cambridge University Press, 1999.
9. H. J. Kreuzer, R. Teshima. Time evolution and thermalization of an ideal gas in a box. *Can. J. Phys.* **55**, 189 (1977)
10. T. Mortia, Y. Fukui. Thermalization of the ideal gas in a one-dimensional box. *Can. J. Phys.* **57**, 1103 (1079).
11. N. Penkova, M. Petrova, E. Shandurkov, B. Borisova, D. Mladenova, A. Syunetchieva. Modeling and numerical simulation of basic thermodynamic process of ideal gases. *Sci. Eng. Ed.* **2**, 31 (2017).
12. P. W. Kuchel, R. J. Vaughan. Average lengths of chords in a square. *Math. Mag.* **54**, 261-269 (1981).
13. R. Nandkishore, D. A. Huse. Many-body localization and thermalization in quantum statistical mechanics. *Annu. Rev. Condens. Matter Phys.* **6**, 15-38 (2015).
14. Qiao Y, Shang Z. On the second law of thermodynamics: an ideal-gas flow spontaneously induced by a locally nonchaotic energy barrier. *Physica A* **647**, 129828 (2024)
<https://doi.org/10.1016/j.physa.2024.129828>

15. Qiao Y, Shang Z. Producing useful work in a cycle by absorbing heat from a single thermal reservoir: An investigation on a locally nonchaotic energy barrier. *Physica A* **596**, 127105 (2022)
16. Y. Qiao, Z. Shang, R. Kou. Molecular-sized outward-swinging gate: Experiment and theoretical analysis of a locally nonchaotic barrier. *Phys. Rev. E* **104**, 064133 (2021)
<https://doi.org/10.1103/PhysRevE.104.064133>
17. The computer programs used in the current investigation are available at
http://mmrl.ucsd.edu/Z_Upload/Papers/SupplMater_KnudsenGas.zip
18. S. Lepri, R. Livi, A. Politi. Heat conduction in chains of nonlinear oscillators. *Phys. Rev. Lett.* **78**, 1896 (1997).
19. D. Alonso, A. Ruiz, I. de Vega. Polygonal billiards and transport: diffusion and heat conduction. *Phys. Rev. E* **66**, 066131 (2002).
20. R. Livi, S. Lepri. Heat in one dimension. *Nature* **421**, 327 (2003).
21. B. Li, G. Casati, J. Wang, T. Prosen. Fourier law in the alternate-mass hard-core potential chain. *Phys. Rev. Lett.* **92**, 254301 (2004).
22. A. Tenenbaum, G. Ciccotti, R. Gallico. Stationary nonequilibrium states by molecular dynamics: Fourier's law. *Phys. Rev. A* **25**, 2778 (1982).
23. M. Mareschal, E. Kestemont, F. Baras, E. Clementi, G. Nicolis. Nonequilibrium states by molecular dynamics: transport coefficients in constrained fluids. *Phys. Rev. A* **35**, 3883 (1987).
24. E. E. Tahiri, M. Tij, A. Santos. Monte Carlo simulation of a hard-sphere gas in the planar Fourier flow with a gravity field. *Molecular Phys.* **98**, 239-248 (2000).
25. J. C. Maxwell. *Theory of Heat* (Longmans, Green, and Co., London, 1872), p. 300
26. R. P. Feynman, R. B. Leighton, M. Sands. *The Feynman Lecture Notes on Physics*, Vol. 1, Chapt. 46 (Basic Books, 2011)
27. H. S. Leff, A. F. Rex. *Maxwell's Demon: Entropy, Information, Computing* (Princeton Univ. Press, 1990)
28. T. Sagawa, M. Ueda, Second law of thermodynamics with discrete quantum feedback control. *Phys. Rev. Lett.* **100**, 080403 (2008)
29. C. Jarzynski. Nonequilibrium equality for free energy differences. *Phys. Rev. Lett.* **78**, 2690 (1997).

30. J. C. Maxwell. On the dynamical theory of gases. *London Edinburgh Dublin Phil. Mag. J. Sci.* **35**, 215, 1868
31. J. C. Maxwell. The dynamic evidence of the molecular constitution of bodies. In: W. D. Niven (ed.), *The Scientific Papers of James Clerk Maxwell Vol. 2* (Cambridge Univ. Press, 2010) p. 434.
32. T Wu, D Zhang. Impact of adsorption on gas transport in nanopores. *Scientific Reports* **6**, 23629 (2016)
33. A. Han, V. K. Punyamurtula, Y. Qiao. Heat generation associated with pressure-induced infiltration in a nanoporous silica gel. *J. Mater. Res.* **23**, 1902 (2008).
34. A. Han, W. Lu, V. K. Punyamurtula, T. Kim, Y. Qiao. Temperature variation in liquid infiltration and defiltration in a MCM41. *J. Appl. Phys.* **105**, 024309 (2009).
35. B. J. Hinds, N. Chopra, T. Rantell, R. Andrews, V. Ravalas, L. G. Bachas. Aligned multiwalled carbon nanotube membranes. *Science* **303**, 62 (2004).
36. A. A. Gusev, O. Guseva. Rapid mass transport in mixed matrix nanotube/polymer membranes. *Adv. Mater.* **19**, 2672 (2007).
37. Han A, Lu W, Punyamurtula VK, Chen X, Surani FB, Kim T, Qiao Y. Effective viscosity of glycerin in a nanoporous silica gel. *J. Appl. Phys.* **104**, 124908 (2008).